A Moment-based Polarimetric Radar Forward Operator for Rain Microphysics

Matthew R. Kumjian* and Charlotte P. Martinkus

Department of Meteorology and Atmospheric Science, The Pennsylvania State University, University Park, Pennsylvania, USA

Olivier P. Prat

North Carolina Institute for Climate Studies, North Carolina State University, Asheville, North Carolina, USA

Scott Collis

Argonne National Laboratory, Chicago, Illinois, USA

Marcus van Lier-Walqui

Center for Climate Systems Research, Columbia University, and NASA Goddard Institute for Space Studies, New York, New York, USA

Hugh C. Morrison

National Center for Atmospheric Research†, Boulder, Colorado, USA

**Corresponding author address:* Department of Meteorology and Atmospheric Science, The Pennsylvania State University, 513 Walker Building, University Park, PA 16802

E-mail: kumjian@psu.edu

†NCAR is supported by the National Science Foundation

ABSTRACT

There is growing interest in combining microphysical models and polarimetric radar observations to improve our understanding of storms and precipitation. Mapping model-predicted variables into the radar observational space necessitates a forward operator, which requires assumptions that introduce uncertainties into model-observation comparisons. These include uncertainties arising from the microphysics scheme *a priori* assumptions of a fixed drop size distribution (DSD) functional form, whereas natural DSDs display far greater variability. To address this concern, this study presents a moment-based polarimetric radar forward operator with no fundamental restrictions on the DSD form by linking radar observables to integrated DSD moments. The forward operator is built upon a dataset of $>$ 200 million realistic DSDs from one-dimensional bin microphysical rain shaft simulations, and surface disdrometer measurements from around the world. This allows for a robust statistical assessment of forward operator uncertainty and quantification of the relationship between polarimetric radar observables and DSD moments. Comparison of "truth" and forward-simulated vertical profiles of the polarimetric radar variables are shown for bin simulations using a variety of moment combinations. Higher-order moments (especially those optimized for use with the polarimetric radar variables: the 6th and 9th) perform better than the lower-order moments (0th and 3rd) typically predicted by many bulk microphysics schemes.

1. Introduction

There is growing interest in combining numerical models and observations to further our understanding of weather and climate. For microphysical comparisons, polarimetric Doppler radar is a particularly attractive choice of observations, owing to the fact that these data can provide several key pieces of information useful for characterizing bulk properties of precipitation, such as hydrometeor sizes, shapes, concentrations, and motion (Kumjian 2013a). Radar data resolution is also ideal because it can match or exceed the higher resolution of many mesoscale and storm-scale model outputs (Keil et al. 2003). Radar data have been useful for a variety of purposes, including for model evaluation (e.g., Hagos et al. 2014; Sinclair et al. 2016; Barnes and Houze 2016; Johnson et al. 2016), data assimilation (e.g., Tong and Xue 2005; Jung et al. 2010b; Schenkman et al. 2011; Putnam et al. 2014), and gaining insights about precipitation microphysical processes (e.g., Kumjian and Ryzhkov 2010, 2012; Dawson et al. 2014; Kumjian et al. 2014; Sulia and Kumjian 2017a,b). To make such comparisons within the variable space of observations, forward operators must be used to convert model-predicted variables into quantities observed by some radar platform.

Several polarimetric radar forward operators have been developed for use with bulk and bin microphysics models (e.g., Pfeifer et al. 2008; Jung et al. 2008; Ryzhkov et al. 2011; Andrić et al. 2013). For bulk models, without exception the approach is to use model-predicted microphysical quantities to construct a particle size distribution (PSD) for each hydrometeor type at each grid box that matches the microphysics scheme's underlying assumptions about the PSD functional form. Most often, the PSDs (including raindrop size distributions, or DSDs) are given by gamma or normalized gamma functions (e.g., Willis 1984; Testud et al. 2001). The PSD is then discretized into a series of particle size bins, whereupon electromagnetic scattering calculations are performed (e.g., Ryzhkov et al. 2011). The hydrometeor scattering properties and PSD are then integrated to obtain the radar variables of interest at each grid box.

This approach has been successful in producing simulated fields of polarimetric radar variables that reproduce basic observed signatures, particularly in convective storms (e.g., Jung et al. 2010a; Ryzhkov et al. 2011, 2013a,b; Kumjian et al. 2012, 2014, 2015; Putnam et al. 2014, 2017; Dawson et al. 2014; Johnson et al. 2016) and winter storms (e.g., Andrić et al. 2013; Sulia and Kumjian 2017a,b). However, these model-observation comparisons using forward operators often have substantial uncertainties, the details of which usually are not assessed. One class of uncertainties includes those associated with tunable parameters used or imposed by the forward operator to characterize particle properties not explicitly predicted or diagnosed by the microphysics model; for example, ice crystal shapes are treated using fixed maximum dimension-thickness relationships in the forward operators of Ryzhkov et al. (2011) and Andrić et al. (2013). Other examples include particle fall behaviors (i.e., particle orientation can strongly affect the simulated radar variables but typically is not predicted or provided by microphysics schemes), and even the choice of electromagnetic scattering calculations employed. An example of the latter is discussed by Schrom and Kumjian (2018), who quantified large errors in simulated polarimetric radar variables when homogeneous spheroids are used to approximate branched planar crystals like dendrites and stellars in scattering calculations.

Another class of uncertainties in model-observation comparison arises only when comparing to the observations themselves, originating from structural errors associated with the accuracy of approximations explicitly made in the formulation of the microphysics schemes. For example, most bulk microphysics parameterization schemes assume a functional form for the PSD, typically one that facilitates analytic integration (like the gamma PSD mentioned above). This leads to a unique mapping between model-predicted variables (e.g., total number concentration, total mass content) and radar observational quantities. Real PSDs, however, have much greater variability (i.e., not all PSDs have shapes well defined by the simple analytic PSDs assumed in most bulk schemes), leading to a greater number of degrees of freedom than bulk schemes are able to represent. In other words, although there is a unique mapping between PSD moments and radar variables for most bulk microphysics schemes, no such relationship exists in nature[1] (with the exception of a nearly unique mapping between the sixth moment of the raindrop size distribution and radar reflectivity). This necessitates a treatment that accounts for this model deficiency in order to make valid comparisons between radar variables resulting from real and simulated PSDs.

This paper circumvents the problem of imposed PSD shape by creating a moment-based forward operator: one that does not assume any PSD functional form. The moment-based forward operator developed herein is flexible and can be used with a variety of bulk microphysics schemes: it directly connects the polarimetric radar variables to integrated PSD moments, regardless of the underlying PSD functional form assumed in such schemes. For example, traditional two-moment bulk microphysics schemes predict mixing ratios for mass (proportional to the third moment) and total number (the zeroth moment). Inputs from such a scheme for the forward operator are values of the zeroth and third moments at each model grid point, with no assumptions about the underlying PSD shape. Note that the moment-based approach is *necessary* in order to use instrument forward operators with bulk microphysics schemes that do not assume an underlying functional PSD form (e.g., Chen and Liu 2004; Szyrmer et al. 2005; Laroche et al. 2005; Kogan and Belochitski 2012). For most current bulk microphysics schemes that *do* use a fixed PSD functional form, our moment-based forward operator also provides an estimate of uncertainty owing to natural PSD variability not accounted for in these schemes. Such a framework is also

[1]Note that these uncertainties are also relevant to the calculation of microphysical process rates; however, this is beyond the scope of the current study and will be addressed in future work.

used to find the optimal combinations of moments that minimize uncertainty in mapping to the radar variables. This can help guide the choice of prognostic variables in bulk schemes such that they are optimized for use in conjunction with radar observations.

Our study is the first step towards this moment-based approach, using the simplest framework: rain (liquid-only) microphysics. Unlike the uncertainties and complexities associated with snow crystals described above, raindrop shapes are relatively well understood (e.g., Pruppacher and Pitter 1971; Beard 1976; Beard and Chuang 1987; Brandes et al. 2005; Thurai et al. 2009), as are their electromagnetic scattering properties at weather radar wavelengths (e.g., Bringi and Chandrasekar 2001; Ryzhkov et al. 2011). Additionally, dual-polarization radar variables are known to provide information – at least qualitatively – on rain microphysical processes such as evaporation (Li and Srivastava 2001; Kumjian and Ryzhkov 2010; Xie et al. 2016), size sorting (Kumjian and Ryzhkov 2012), and collision-coalescence-breakup (Kumjian and Prat 2014). In developing this moment-based forward operator, we also present the relationships between integrated DSD moments and the polarimetric radar variables, and quantify the uncertainty associated with DSD shape in terms of the polarimetric radar variables for broader use.

The next section outlines the methods used in this study. Section 3 describes how to identify the optimal prognostic moments for use with polarimetric radar data. The forward operator is developed in section 4. Section 5 shows example tests using a simulated rain shaft. The paper closes with a discussion and summary of the main conclusions in section 6.

2. Methods

DSDs are the key to linking microphysical model output to radar data because they are used to compute the bulk physical quantities of interest predicted by the model, typically total number and mass mixing ratios, as well as the radar variables, such as equivalent reflectivity factor at horizontal polarization (Z_H), differential reflectivity (Z_{DR}), and specific differential phase (K_{DP}). For a review of these dual-polarization radar variables, see Kumjian (2013a,b) and Kumjian (2018) and references therein.

The first step towards developing the forward operator is to create a database of DSDs. A large population of DSDs is desired because the forward operator should be able to handle any realistic precipitation situation. DSDs from both state-of-the-art bin model simulations and ground-based disdrometers are used (described below). The simulations allow for DSDs from a wide portion of the parameter space, representative of a diverse set of precipitation regimes, whereas the disdrometer data include DSDs from several different geographic regions.

The dataset will be briefly described here; details are provided in Morrison et al. (2018). Disdrometer data from the U.S. Department of Energy (DOE) Atmospheric Radiation Measurement (ARM) program Climate Research Facility are used (Ackerman and Stokes 2003; Mather and Voyles 2013). These include samples from model RD80 Joss-Waldvogel impact disdrometers (e.g., Joss and Waldvogel 1967) and two-dimensional video disdrometers (2DVD; e.g., Tokay et al. 2001; Kruger and Krajewski 2002). The data come from geographically diverse regions, including ARM permanent sites in the U.S. Southern Great Plains, Tropical Western Pacific, and Eastern North Atlantic (Mather and Voyles 2013; Sisterson et al. 2016; Long et al. 2016, respectively), as well as field campaigns in the Indian Ocean (Yoneyama et al. 2013; Gottschalck et al. 2013), and Finland (see Miller et al. 2016; Petäjä et al. 2016). These data cover all months and seasons, including stratiform, convective, continental, and maritime regimes. Data quality control and filtering procedures are described in Morrison et al. (2018). After these procedures, 671 303 disdrometer DSD samples remain (a sample is a 30− or 60−second average).

The simulations used herein employ the one-dimensional spectral bin microphysical model of Prat and Barros (2007) and Prat et al. (2012), following the setup used by Kumjian and Prat

(2014). DSD evolution is explicitly predicted for one hour in a one-dimensional, 3-km tall rain shaft with 10-m vertical grid spacing. The model is initialized with a prescribed DSD at the top of the domain. At the first time step, the raindrops (which are discretized into 40 size bins) begin to fall and the DSD then freely evolves under the influence of microphysical processes. The model considers interactions among raindrops including drop coalescence, collisional and aerodynamic breakup, and sedimentation. Overall, the model performs well, consistently able to reproduce realistic DSDs as compared to radar and disdrometers (Prat et al. 2008; Prat and Barros 2009; Kumjian and Prat 2014). One potential bias exists for very heavy rainfall ($>$ 100 mm hr^{-1}), in which an overly aggressive drop breakup formulation may result in an underestimate of median drop size (Kumjian and Prat 2014). A total of 10 742 simulations were performed, covering a wide range of initial conditions, including rainfall intensity, mean drop size, DSD shape, etc. (details can be found in Morrison et al. 2018). To populate the DSD dataset, DSDs are taken at every model height and output time (every 1 minute). Doing so allows us to obtain samples of transient and non-steady-state DSDs from processes such as size sorting that are not well captured in disdrometer data, but are readily observed in dual-polarization radar observations (e.g., Kumjian and Ryzhkov 2012). The bin simulations produced 184 180 279 DSDs. Thus, the combined dataset is strongly dominated by the bin simulations owing to their availability.

Many of the model-predicted physical quantities of interest are proportional to specific moments of the DSD:

$$M_k \equiv \int_{D_{\min}}^{D_{\max}} N(D) D^k dD \tag{1}$$

where M_k is the k^{th} moment of the DSD, integrated from the minimum drop size $D_{\min}$ to maximum drop size $D_{\max}$, and $N(D)$ is the DSD (number concentration of drops with diameters in the size range D to $D+dD$). For example, the zeroth moment (M_0) of the DSD is the raindrop total number concentration, whereas the third (M_3) is proportional to the total raindrop mass content. For each DSD in the dataset, the integer moments $k = [0,10]$ were computed using eqn (1). Because the moment values may span several orders of magnitude, we convert them to decibels (dB) using

$$M_k\,[\mathrm{dB}] = 10 \times \log_{10}\left(\frac{M_k\,[\mathrm{mm}^k\ \mathrm{m}^{-3}]}{1\ \mathrm{mm}^k\ \mathrm{m}^{-3}}\right) \tag{2}$$

Note that the units depend on moment order k. The moment values will be expressed in dB for the remainder of the paper. In the current paper, we relate the polarimetric radar variables computed from observed and simulated DSDs to their respective moments. The moments themselves display natural covariability that lends itself to scaling relationships and a general DSD normalization method discussed in further detail in Morrison et al. (2018). All calculations are performed at S band ($\sim$11-cm wavelength), assuming liquid drops at 20 °C and are valid for low radar antenna elevation angles ($< 10°$). The raindrop shapes are taken as a function of size following Brandes et al. (2005). The T-matrix method (Mishchenko 2000) is used to compute the forward and backward scattering amplitudes, from which the radar variables are calculated following Ryzhkov et al. (2011). This is the same method employed by Kumjian and Prat (2014) and numerous other studies.

As mentioned in the introduction, we have not explored the effect of other sources of uncertainty such as choice of drop shape model, liquid water temperatures, and distribution of canting angles − we have focused solely on the uncertainty associated with the mapping between model-predicted quantities (integrated DSD moments) and polarimetric radar variables that is related to natural DSD variability. Uncertainty not estimated here can be easily added in subsequent work by summation of variances, assuming no correlation between different error terms. Thurai et al. (2007) showed that, at S band, the discrepancies in Z_H and K_{DP} arising from different choices of raindrop shape models and liquid water temperature are negligible, whereas Z_{DR} differences could be up to $0.1-0.2$ dB in magnitude for a small subset of DSDs characterized by large median drop sizes. For most of the DSD parameter space considered by our forward operator, then, we expect the added uncertainty arising from these choices to be smaller than the spread in Z_{DR} values arising owing to natural variability.

Figures 1-3 show the joint histograms of M_0 through M_{10} versus the polarimetric radar variables using all DSDs in the dataset. These figures reveal the relationships between polarimetric radar variables and moments of different order k. As expected, some moments exhibit much clearer relationships with the radar variables than others. For example, Z_H is nearly perfectly described by M_6, whereas the dependence on M_0 is rather weak (Fig. 1). This is expected given that M_6 defines the radar reflectivity factor for spherical liquid drops with diameters small compared to the radar wavelength; at S band, most drops are safely considered electromagnetically small. That is to say, the Rayleigh approximation holds for all but the largest raindrops, where minor deviations from a linear $Z_H - M_6$ relationship arise. K_{DP} (Fig. 3) appears closely related to M_4 and M_5 as suggested in previous studies (e.g., Sachidananda and Zrnić 1986; Bringi and Chandrasekar 2001; Lee et al. 2004; Maki et al. 2005). This is in sharp contrast to Z_{DR}, which has more tenuous relationships with the moments, with higher-order moments displaying only slightly stronger relationships to Z_{DR} (Fig. 2). In part, these weak relationships are because Z_{DR} does not depend on raindrop concentration, whereas Z_H and K_{DP} do.

These joint histograms have implications for which prognostic moments offer the greatest utility for linking model output with the polarimetric radar variables. M_0, for example, has a broad distribution for all three radar variables compared to higher-order moments. This implies a wide range of M_0 values can produce the same Z_H, Z_{DR}, or K_{DP} values. As such, M_0 has limited utility in informing Z_H, Z_{DR}, or K_{DP} compared to higher-order moments. From the perspective of model validation as well as data assimilation, the best prognostic DSD moments are likely to be those most directly informed by observed radar quantities; in that context, the standard choice of M_0 and M_3 in bulk microphysics schemes is unfortunate, as these moments are only weakly related to radar variables. This motivates the following question: which combination of moments offer the greatest information content (i.e., least spread in the joint histograms) for the radar variables? The next section addresses this question.

3. Identifying Optimal Predicted Moments for Polarimetric Radar Measurements

Though bulk microphysics schemes typically predict M_0 and M_3, the S-band radar variables are strongly related to higher moments in part because the back- and forward-scattering cross sections are proportional to D^6 for particles with diameters small compared to the radar wavelength. This leads to challenges in comparing radar observations with microphysical model output. Here we assess which pair of moments (i.e., for a two-moment scheme) minimizes the variability in Z_H, Z_{DR}, and K_{DP} for a collection of realistic DSDs, and thus would offer the most information content on those radar variables if prognosed.

We first discretize the pair of moments M_k and M_j into 1-dB $\times$ 1-dB bins. Within each bin, the Z_H, Z_{DR}, or K_{DP} values from the DSD dataset are collected. For example, in Fig. 4a, an arbitrary bin is selected, within which M_0 values range between $30-31$ dB and M_3 values between $32-33$ dB. Within this bin, there are $\sim 2.2 \times 10^5$ DSDs, with the bulk of their corresponding Z_H values ranging from 35 to 46 dBz (Fig. 4b). We can quantify the spread of Z_H values within each pixel by calculating the standard deviation. However, before computing the standard deviation of Z_H values, the evident linear trends (in logarithmic space) must be removed. Otherwise, variability within this bin will be a result of the linear trend, as opposed to the variability *about* this linear trend. Thus, for each 1-dB $\times$ 1-dB bin, linear trends in Z_H with M_0 and M_3 across this bin are removed. The standard deviation is then computed, resulting in a 2-dimensional map of detrended standard deviation σ_{Z_H} spanning the range of moment values (not shown).

To objectively quantify variability in prognostic moment pairs, we define a variable ξ:

$$\xi \equiv \sum_{m}^{M} \sum_{n}^{N} \sigma_X \left[M_k^{(m)}, M_j^{(n)} \right] \times P \left[M_k^{(m)}, M_j^{(n)} \right] \tag{3}$$

where M and N are the number of bins for discretized moments M_k and M_j, respectively; σ_X is the standard deviation of the detrended polarimetric radar variable X for the m^{th} bin of M_k and n^{th} bin of M_j, and P is the joint normalized probability distribution function (PDF) of moments M_k and M_j in bins m and n, respectively. Physically, ξ represents the PDF-weighted spread in a given radar variable for a given pair of moments (M_k, M_j). Note that K_{DP} is expressed in dB for these calculations to facilitate comparison with Z_H and Z_{DR}.

The PDF weighting ensures that contributions from rare or outlier pixels are commensurate with their occurrence. However, the PDF generated by the bin simulations and disdrometer data is arbitrary (based on availability of disdrometer data and locations, choice of bin simulation parameter space, etc.) and thus may inadvertently introduce biases if used as is. Instead, a climatology of observed rainfall rates from 5-minute ground-based rain gauges (see Morrison et al. 2018) is used to subsample the DSD dataset. This provides a dataset of 2×10^5 DSDs that has approximately equal contributions from the disdrometer and bin simulations and that reflects the climatological distribution of rainfall rates in the U.S. as measured from ground-based gauges.

The resulting ξ maps are shown in Figure 5. One can see that ξ is minimized for different pairs of moments for Z_H, Z_{DR}, and K_{DP}. This is expected, given that each variable has different dependencies on the DSD. For example, given that Z_H is nearly equal to M_6 at S band, most combinations of M_6 and another moment provide the lowest ξ values (Fig. 5a). In contrast, (M_5, M_9) produces the lowest ξ for Z_{DR} (Fig. 5b). Also note the large ξ values for moment order less than or equal to M_3, which reveals large variability in the radar variables for the moments traditionally predicted by bulk microphysics schemes. To identify the moment pair that minimizes variability for all three variables, $\xi(Z_H)$, $\xi(Z_{\mathrm{DR}})$, and $\xi(K_{\mathrm{DP}})$ were normalized by their respective mean values and summed together (Fig. 5d). The moment pair that yielded the minimum variability[2] and thus is determined to be the optimum moment pair for informing models with dual-polarization radar observations was found to be (M_6, M_9). For the remainder of the paper, we will show traditional prognosed moments (M_0, M_3) and the ones indicated by this analysis (M_6, M_9). Additionally, given the practical consideration of predicting M_3 in bulk microphysics schemes (as it is proportional to total mass), (M_3, M_6) will be shown as well. Unlike M_0, M_3, and M_6, M_9 has no conventional physical meaning[3] other than the ninth moment of the DSD.

4. The Moment-based Forward Operator

The moment-based forward operator is built using the full (combined) dataset rather than the subsampled one. This is because we desire the forward operator to cover the maximum possible spread of moment values, even if these values are rare in nature. We take a lookup table approach to the forward operator: linear interpolation (in logarithmic moment space) of the binned (M_j, M_k) values is used as a function of the input moment values. Then, the corresponding mean values (in each $1-$dB $\times$ $1-$dB pixel) of Z_H, Z_{DR}, and K_{DP} are found. For example, the two-moment version of the forward operator takes as inputs a given moment pair (M_j,M_k) from, say, output from a two-moment bulk microphysics scheme that predicts M_j and M_k. The mean value for each polarimetric radar variable in the corresponding bin is assigned. Sensitivity tests (not shown) suggested 1-dB

[2]Note: this is somewhat sensitive to how the ξ for each variable are summed. Different weightings may be applied as needed. For example, if less confidence is placed on comparing Z_{DR} to observations owing to calibration issues, or on K_{DP} owing to difficulties in its estimation because of noisy total differential phase (Φ_{DP}) fields, one could weight the summation away from one of the variables in favor of the other two.

[3]If normalized by M_6, then M_9 could be considered the "reflectivity-weighted mass" of the distribution.

$\times$1-dB moment bins were an adequate balance between attaining sufficiently high resolution in the M_j-M_k parameter space and keeping the look-up tables manageable in size for our purposes herein. Note that the forward operator may be easily updated as more DSD data become available (e.g., from ongoing and future field campaigns), or with additional bin model simulations, etc., and can be generated at higher resolutions if needed in future work. A graphical depiction of three versions of the two-moment operator is shown in Fig. 6. The three versions use the (M_0, M_3), (M_3, M_6), and (M_6, M_9) moment pairs, respectively, for the polarimetric radar variables Z_H, Z_{DR}, and K_{DP}. These versions of the forward operator would be used with schemes that predict M_0 and M_3 (most existing two-moment bulk microphysics schemes), M_3 and M_6, and M_6 and M_9, respectively.

The (M_0, M_3) operator (Fig. 6a-c) is based on the moments typically predicted in double-moment bulk microphysics schemes, where M_0 is the total number concentration of drops and M_3 is proportional to the total mass per unit volume of the drops. This version of the forward operator may be used with many commonly used two-moment bulk microphysics schemes, with the inputs simply being the predicted M_0 and M_3 at each model grid point. For the same M_0, we see an increase in Z_H, Z_{DR}, and K_{DP} as M_3 increases. This makes sense physically: as M_3 (mass) of the drops increases for a fixed number concentration, the drops must be increasing in size. A different pattern emerges for the (M_3, M_6) operator (Fig. 6d-f). Because M_6 is almost identically Z_H at S band, there is little change in Z_H for increasing M_3 when M_6 is held fixed. For a given M_3, increasing M_6 leads to larger Z_H, Z_{DR}, and K_{DP}. The (M_6, M_9) operator (Fig. 6g-i) is similar to the (M_3, M_6) operator, though a given value of the radar variables generally is spread over fewer of the $1-$dB by $1-$dB moment bins owing to less natural variability in the (M_6, M_9) moment pair (see Morrison et al. 2018).

Recall that each 1-dB $\times$ 1-dB pixel on these maps contains numerous DSDs and thus a distribution of polarimetric radar variable values within it. A novel feature of our moment-based forward operator is that it facilitates estimating the uncertainty associated with a moment-based approximation of natural DSDs. To compute such uncertainty, the standard deviation, skewness, and kurtosis are computed using the detrended data to characterize the distributions of intrinsic Z_H, Z_{DR}, and K_{DP} variability within each pixel. Figure 7 shows standard deviation of each radar variable distribution within each pixel, for the three forward operators shown in Fig. 6. Comparing the (M_0, M_3) operator (top row) with the (M_3, M_6) and (M_6, M_9) in the rows below, a large reduction in the standard deviation of Z_H is evident, which follows naturally from the fact that (M_3, M_6) and (M_6, M_9) both utilize M_6. There is also a reduction in the standard deviation of Z_{DR} and K_{DP} evident when moving from the top to bottom rows. Skewness magnitude (Fig. 8) and kurtosis (not shown) are also substantially higher for (M_0, M_3), compared with the other moment-pair choices. High skewness magnitude and kurtosis imply that the uncertainty within these regions is *non-Gaussian*. Such non-Gaussianity poses problems for optimal estimation and Kalman-filter based techniques that typically assume model linearity and Gaussian error statistics, with few exceptions (e.g., Hodyss 2011; Amezcua and Leeuwen 2014; Bishop 2016).

5. Examples Using Simulated Rainshafts

To test the effectiveness of the forward operator, example rainshafts from the 1-D bin simulations are used. Radar variables are calculated at each minute directly from the bin model DSDs, which are considered "truth" for these tests. We also compute the moments from these DSDs, which serve as the inputs to the forward operator. The radar variables produced by the forward operator are compared to the truth (bin simulation) values computed directly from the DSD itself. This simulation is independent from the ones used to construct the DSD database.

Figure 9 shows vertical profiles of Z_H, Z_{DR}, and K_{DP} for a bin simulation initialized with a normalized gamma DSD aloft with rainfall rate $R = 36.7$ mm hr^{-1}. The "truth" profiles are shown in blue lines, whereas the (M_6, M_9) forward operator profiles are in gray, with ±1 standard deviation shown as horizontal bars on the forward-simulated profiles every 10 grid points. Each row represents a different output time in the simulation. Each profile shows the evolution of the rain shaft as raindrops fall towards the surface. At early times, size sorting of drops (e.g., Kumjian and Ryzhkov 2012; Kumjian and Prat 2014) is evident by the rapidly increasing Z_{DR} and decreasing Z_H and K_{DP} values at the bottom edge of the rain shaft. This provides a good test for the forward operator given the somewhat exotic DSDs compared to later times when the profiles change little in height.

The forward operator-retrieved Z_H profile nearly perfectly matches the "truth" profiles at each time, which is unsurprising given that M_6 is one of the moments used to inform the forward simulator. Additionally, the standard deviation is very small at all heights, as indicated by negligibly small error bars. Thus, not only does the forward operator correctly diagnose Z_H, but it also correctly suggests high confidence in the diagnosis. In contrast to Z_H, Z_{DR} and K_{DP} provide a more difficult challenge for the forward operator given their weaker relationships to DSD moments (cf. Figs. 2 and 3). Nonetheless, the forward operator does a satisfactory job at accurately diagnosing the evolving Z_{DR} and K_{DP} profiles: relative error magnitudes (defined as the difference between the "truth" and forward operator curves) generally are less than 0.5%, 5%, and 10% for Z_H, Z_{DR}, and K_{DP}, respectively. The relatively larger error magnitudes for K_{DP} are a result of using higher-order moments (recall that M_4 and M_5 are the most closely related to K_{DP}). Additionally, the diagnosed profiles are almost always within the ±1 standard deviation bars. For times when the "truth" lies outside the ±1 standard deviation bars, the diagnosed Z_{DR} and K_{DP} values are still well within typical theoretical radar measurement errors of $\sim$0.1-0.2 dB for Z_{DR} and $\sim$0.1-0.2 deg km^{-1} for K_{DP} (Melnikov 2004). Thus, the (M_6, M_9) forward operator performs well for the evolving rain shaft.

Figure 10 compares the performances of three different versions of the forward operator: (M_0, M_3) (Fig. 10a-c), a commonly used pair of prognostic moments for two-moment bulk microphysics parameterization schemes, (M_3, M_6) (Fig. 10d-f), and (M_6, M_9) (Fig. 10g-i). This example uses the same initial DSD aloft as in Fig. 9, with the output time $t = 10$ minutes shown. It is clear that the (M_3, M_6) and (M_6, M_9) versions are both more accurate and have less predicted spread (± 1 standard deviation) than the (M_0, M_3) version, an expected result given the higher moment orders used. In contrast, the less accurate (M_0, M_3) version of the forward operator has relatively larger error bars, indicating that the forward operator correctly assesses lower confidence when it is less accurate. This is a novel feature of the moment-based forward operator presented here. That the "truth" profiles fall outside the forward operator ± 1 standard deviation bars illustrates the low-information content of M_0 and M_3 for the polarimetric radar variables, and is not unexpected, given that approximately 32% of all forward-simulated values will fall outside these bounds, assuming Gaussian error statistics. Furthermore, in the case of (M_0, M_3), Fig. 8 suggests that the standard deviation may not well-characterize errors given strong deviations from Gaussianity.

Figure 11 shows another example; this time, the simulation is initialized with a normalized gamma DSD aloft with much lower rainfall rate ($\sim$0.3 mm hr^{-1}), again one that was not included in the initial dataset. As with the previous example, we see a marked improvement of the forward operator performance going from (M_0, M_3) (Fig. 11a-c) to (M_3, M_6) (Fig. 11d-f) and again to (M_6, M_9) (Fig. 11g-i). Once again, the ± 1 standard deviation bars reflect the increasing forward simulator uncertainty with decreasing accuracy, particularly evident in the (M_0, M_3) version of the operator. The (M_3, M_6) operator works well for Z_H and K_{DP}, but has slight positive bias for Z_{DR}. However, the discrepancy is $\leq 0.1 - 0.2$ dB, which is well within observation error. The superior performance of the (M_6, M_9) operators in both examples suggests it is robust for use in both light and heavier rainfall rates. These results show that using a bulk microphysics scheme that predicts M_3 and M_6 (and/or M_9) instead of M_0 and M_3 is better for use of dual-polarization radar data as a constraint or for data assimilation. Note that including M_3 as a prognostic variable is important for conserving mass in models, so not predicting it may be problematic in practice. Thus, we advocate for models to use M_3 and M_6 as prognostic variables for two-moment schemes, or M_3, M_6, and M_9 as prognostic variables for three-moment schemes. For two-moment bulk microphysics schemes that predict M_0 and M_3, dual-polarization radar data may still be used, just with considerably larger errors and greater uncertainty in the mapping between model-predicted quantities and the observed radar quantities. Whereas our forward operator attempts to quantify this uncertainty, existing forward operators use the model-assumed DSD shape (which forces a unique mapping between the predicted variables and radar variables that does not exist in nature) and does not quantify uncertainties associated with this assumption.

In principle, the approach outlined above can be extended to any number of moments and any radar variable with an accurate DSD-based forward operator. We have tested a three-moment version of the forward operator using M_0, M_3, and M_6, the most common prognosed moments for existing three-moment schemes (e.g., Milbrandt and Yau 2005). The results showed only minimal improvement over (M_3, M_6) and (M_6, M_9) owing to the low-information content of M_0 for radar variables (cf. Figs. 1-3). Higher-order moments (e.g., M_3, M_6, M_9) may be more useful with polarimetric radar variables and are attractive from a microphysical modeling perspective because M_3 (mass) is a prognostic variable, as discussed above. Although some microphysical process rates are strongly dependent on lower-order moments, using the three-moment combination (M_3, M_6, M_9) allows for diagnosing lower-order moments quite well (Morrison et al. 2018) and thus is not a significant concern.

6. Discussion and Summary

A large dataset of disdrometer-estimated and bin-model-simulated DSDs was constructed to quantify the relationships between different integrated moments and the S-band polarimetric radar variables, determine the uncertainty of those radar variables for a given pair of DSD moment values, and develop a moment-based polarimetric radar forward operator. This dataset comprises 671 303 DSDs estimated from Joss-Waldvogel and 2D-video disdrometers at U.S. Department of Energy sites around the world, as well as 184 180 279 DSDs simulated using a one-dimensional bin microphysical model that explicitly treats raindrop collisional processes.

The data reveal a strong relationship between the sixth moment of the DSD (M_6) and radar reflectivity factor at horizontal polarization Z_H, as expected: for spherical liquid droplets with diameters small compared to the radar wavelength, the reflectivity factor is exactly equal to M_6. The specific differential phase K_{DP} was most closely related to M_4 and M_5, as reported in some previous studies (e.g., Sachidananda and Zrnić 1986; Bringi and Chandrasekar 2001; Lee et al. 2004; Maki et al. 2005). In contrast, differential reflectivity Z_{DR} showed no strong relationship with any of the DSD moments, but tended to have slightly reduced spread for higher-order moments. Future work will explore additional observations and their relationships to DSD moments, such as mean Doppler velocity from vertically pointing radar, lidar backscatter, etc.

The dataset was subsampled to 2×10^5 DSDs based on a climatology of observed rainfall in the U.S. (Morrison et al. 2018) to determine the expected natural variability of the radar variables for a given pair of moment values. The pair of moments minimizing this variability is M_6 and M_9. Choosing these optimal moments is a way of recasting DSD variability such that natural variability is minimized in each (M_j, M_k) pixel. In contrast, moments predicted by most bulk microphysical parameterization schemes (M_0 and M_3) revealed much greater variability for the polarimetric radar variables. This implies that, when comparing rain microphysical models and polarimetric radar observations, predicting higher-order moments (as opposed to or in addition to M_0 and M_3) could significantly improve the information content obtained from the radar variables.

A forward operator was developed to relate integrated DSD moments to polarimetric radar variables. The operator provides the mean value of Z_H, Z_{DR}, and K_{DP} for a given pair of moment values as inputs, as well as the uncertainty in the radar variables caused by natural DSD variability (i.e., the detrended standard deviation in Z_H, Z_{DR}, and K_{DR} within a M_j-M_k bin), and information about the distribution of radar variable values (i.e., the skewness and kurtosis). Using one-dimensional rainshafts as a benchmark, several different versions of two-moment forward operators were tested: (M_0, M_3), (M_3, M_6), and (M_6, M_9). The (M_6, M_9) version performed well for different rainshafts of varying rainfall rate, including more exotic DSDs arising from size sorting early in the rainshaft evolution. In contrast, the forward operators with lower moment orders performed worse. The forward operator also correctly predicted its uncertainty, with greater variability indicated for the less accurate versions. This is a novel aspect of the operator developed herein.

The optimal moments for informing on the dual-polarization radar variables are of higher order than bulk microphysics schemes typically prognose. Though such high moments individually may not provide much of a constraint for lower-order moments needed for such schemes, they can still reduce the uncertainty considerably when used in combination (i.e., multiple prognostic moments) and/or in combination with lower-order moments (Morrison et al. 2018). In other words, if attempting to diagnose the kth moment M_k, reference moment M_{k+n} always provides a better estimate than reference moment M_{k-n} for all n. Further, Morrison et al. (2018) show that a three-moment normalization using M_3, M_6, and M_9 will result in only $\sim$21% of the variability in M_0 compared to not using the DSD normalization. Thus, use of such higher-order moments in bulk microphysics schemes may not be detrimental, and indeed could be beneficial when combined with lower-order moments typically prognosed (like M_3).

The moment-based forward operator developed herein is necessary for coupling radar observations with bulk microphysics schemes that do not assume a DSD functional form (e.g., Chen and Liu 2004; Szyrmer et al. 2005; Laroche et al. 2005; Kogan and Belochitski 2012). Other forward operators reliant on a discretized DSD would require assuming an explicit DSD functional form, imposing structural error into the mapping between model output and radar observations. The approach herein strives to minimize and quantify this type of uncertainty, such that the majority of the remaining uncertainty contained in the forward operator arises owing to DSD natural variability, and is explicitly estimated. Ultimately, this type of approach should lead to improved mapping of model output to the radar observational parameter space with a better characterization of uncertainty. For traditional bulk microphysics schemes, use of the moment-based operator described here may prevent errors associated with overconfidently comparing approximate bulk schemes to observations associated with more complex, realistic DSDs.

Acknowledgments. This work was funded by U.S. DOE Atmospheric System Research grant DE-SC0016579. The National Center for Atmospheric Research is sponsored by the National Science Foundation. Disdrometer data were obtained from the Atmospheric Radiation Measurement (ARM) Climate Research Facility Data Archive in Oak Ridge, Tennessee, USA, compiled and maintained by M. Bartholomew. Argonne National Laboratory's work was supported by the U.S. Department of Energy, Office of Science, Office of Biological and Environmental Research, under Contract DE-AC02-06CH11357. We thank the anonymous reviewers for their helpful suggestions and comments that improved the clarity of the manuscript.

References

Ackerman, T. P., and G. M. Stokes, 2003: The Atmospheric Radiation Measurement program. *Phys. Today*, **56**, 38–44.

Amezcua, J., and P. J. V. Leeuwen, 2014: Gaussian anamorphosis in the analysis step of the EnKF: a joint state-variable/observation approach. *Tellus A: Dyn. Meteor. Ocean.*, **66**, 18 pp.

Andrić, J., M. R. Kumjian, D. S. Zrnić, J. M. Straka, and V. M. Melnikov, 2013: Polarimetric signatures above the melting layer in winter storms: An observational and modeling study. *J. Appl. Meteor. Climatol.*, **52**, 682–700.

Barnes, H. C., and R. A. Houze, 2016: Comparison of observed and simulated spatial patterns of ice microphysical processes in tropical oceanic mesoscale convective systems. *J. Geophys. Res.*, **121**, 8269–8296.

Beard, K. V., 1976: Terminal velocity and shape of cloud and precipitation drops aloft. *J. Atmos. Sci.*, **33**, 851–864.

Beard, K. V., and C. Chuang, 1987: A new model for the equilibrium shape of raindrops. *J. Atmos. Sci.*, **44**, 1509–1524.

Bishop, C. H., 2016: The GIGG-EnKF: ensemble Kalman filtering for highly skewed non-negative uncertainty distributions. *Quart. J. Roy. Meteor. Soc.*, **142**, 1395–1412.

Brandes, E. A., G. Zhang, and J. Vivekanandan, 2005: Corrigendum. *J. Appl. Meteor.*, **44**, 186.

Bringi, V. N., and V. Chandrasekar, 2001: *Polarimetric Doppler Weather Radar*. 1st ed., Cambridge University Press, 636 pp.

Chen, J.-P., and S.-T. Liu, 2004: Physically based two-moment bulk water parameterization for warm-cloud microphysics. *Quart. J. Roy. Meteor. Soc.*, **130**, 51–78.

Dawson, D. T., E. R. Mansell, Y. Jung, L. J. Wicker, and M. R. Kumjian, 2014: Low-level ZDR signatures in supercell forward flanks: The role of size sorting and melting of hail. *J. Atmos. Sci.*, **71**, 276–299.

Gottschalck, J., P. E. Roundy, C. J. Schreck, A. Vintzileos, and C. Zhang, 2013: Large-scale atmospheric and oceanic conditions during the 2011-12 DYNAMO field campaign. *Mon. Wea. Rev.*, **141**, 4173–4196.

Hagos, S., Z. Feng, C. D. Burleyson, K.-S. S. Lim, C. N. Long, D. Wu, and G. Thompson, 2014: Evaluation of convection-permitting model simulations of cloud populations associated with the Madden-Julian Oscillation using data collected during the AMIE/DYNAMO field campaign. *J. Geophys. Res. Atmos.*, **119**, 12 052–12 068.

Hodyss, D., 2011: Ensemble state estimation for nonlinear systems using polynomial expansions in the innovation. *Mon. Wea. Rev.*, **139**, 3571–3588.

Johnson, M., Y. Jung, D. T. Dawson, and M. Xue, 2016: Comparison of simulated polarimetric signatures in idealized supercell storms using two-moment bulk microphysics schemes in WRF. *Mon. Wea. Rev.*, **144**, 971–996.

Joss, J., and A. Waldvogel, 1967: A spectrograph for raindrops with automatic interpretation. *Pure Appl. Geophys.*, **68**, 240.

Jung, Y., M. Xue, and G. Zhang, 2010a: Simulations of polarimetric radar signatures of a supercell storm using a two-moment bulk microphysics scheme. *J. Appl. Meteor. Climatol.*, **49**, 146–163.

Jung, Y., M. Xue, and G. Zhang, 2010b: Simultaneous estimation of microphysical parameters and the atmospheric state using simulated polarimetric radar data and an ensemble Kalman filter in the presence of an observation operator error. *Mon. Wea. Rev.*, **138**, 539–562.

Jung, Y., G. Zhang, and M. Xue, 2008: Assimilation of simulated polarimetric radar data for a convective storm using the ensemble Kalman filter. Part I: Observation operators for reflectivity and polarimetric variables. *Mon. Wea. Rev.*, **136**, 2228–2245.

Keil, C., A. Tafferner, H. Mannstein, and U. Schlättler, 2003: Evaluating high-resolution model forecasts of European winter storms by use of satellite and radar observations. *Wea. Forecasting*, **18**, 732–747.

Kogan, Y. L., and A. Belochitski, 2012: Parameterization of cloud microphysics based on full integral moments. *J. Atmos. Sci.*, **69**, 2229–2242.

Kruger, A., and W. F. Krajewski, 2002: Two-dimensional video disdrometer: A description. *J. Atmos. Oceanic Technol.*, **19**, 602–617.

Kumjian, M. R., 2013a: Principles and applications of dual-polarization weather radar. Part I: Description of the polarimetric radar variables. *J. Operational Meteor.*, **1 (19)**, 226–242, doi: 10.15191/nwajom.20130119.

Kumjian, M. R., 2013b: Principles and applications of dual-polarization weather radar. Part II: Warm- and cold-season applications. *J. Operational Meteor.*, **1 (20)**, 243–264, doi:10.15191/nwajom.20130120.

Kumjian, M. R., 2018: Weather radars. *Remote Sensing of Clouds and Precipitation*, C. Andronache, Ed., Springer-Verlag, 1–48.

Kumjian, M. R., S. M. Ganson, and A. V. Ryzhkov, 2012: Freezing of raindrops in deep convective updrafts: A microphysical and polarimetric model. *J. Atmos. Sci.*, **69**, 3471–3490.

Kumjian, M. R., A. P. Khain, N. Benmoshe, E. Ilotoviz, A. V. Ryzhkov, and V. T. J. Phillips, 2014: The anatomy and physics of ZDR columns: Investigating a polarimetric radar signature with a spectral bin microphysical model. *J. Appl. Meteor. Climatol.*, **53**, 1820–1843.

Kumjian, M. R., Z. J. Lebo, and H. C. Morrison, 2015: On the mechanisms of rain formation in an idealized supercell storm. *Mon. Wea. Rev.*, **143**, 2754–2773.

Kumjian, M. R., and O. P. Prat, 2014: The impact of raindrop collisional processes on the polarimetric radar variables. *J. Atmos. Sci.*, **71**, 3052–3067.

Kumjian, M. R., and A. V. Ryzhkov, 2010: The impact of evaporation on polarimetric characteristics of rain: Theoretical model and practical implications. *J. Appl. Meteor. Climatol.*, **49**, 1247–1267.

Kumjian, M. R., and A. V. Ryzhkov, 2012: The impact of size sorting on the polarimetric radar variables. *J. Atmos. Sci.*, **69**, 2042–2060.

Laroche, S., W. Szyrmer, and I. Zawadzki, 2005: A microphysical bulk formulation based on scaling normalization of the particle size distribution. Part II: Data assimilation into physical processes. *J. Atmos. Sci.*, **62**, 4222–4237.

Lee, G. W., I. Zawadzki, W. Szyrmer, D. Sempere-Torres, and R. Uijlenhoet, 2004: A general approach to double-moment normalization of drop size distributions. *J. Appl. Meteor.*, **43**, 264–281.

Li, X., and R. C. Srivastava, 2001: An analytical solution for raindrop evaporation and its application to radar rainfall measurements. *J. Appl. Meteor.*, **40**, 1607–1616.

Long, C. N., J. H. Mather, and T. P. Ackerman, 2016: The ARM Tropical Western Pacific (TWP) Sites. *Meteor. Monogr.*, **57**, 7.1–6.14.

Maki, M., S.-G. Park, and V. N. Bringi, 2005: Effect of natural variations in rain drop size distributions on rain rate estimators of 3 cm wavelength polarimetric radar. *J. Meteor. Soc. Japan*, **83**, 871–893.

Mather, J. H., and J. M. Voyles, 2013: The ARM Climate Research Facility: A review of structure and capabilities. *Bull. Amer. Meteor. Soc.*, **94**, 377–392.

Melnikov, V. M., 2004: Simultaneous tranmission mode for the polarimetric wsr-88d. *NOAA/NSSL Rep.*, 84 pp.

Milbrandt, J. A., and M. K. Yau, 2005: A multimoment bulk microphysics parameterization. Part II: A proposed three-moment closure and scheme description. *J. Atmos. Sci.*, **62**, 3065–3081.

Miller, M. A., K. Nitschke, T. P. Ackerman, W. R. Ferrell, N. Hickmon, and M. Ivey, 2016: The ARM mobile facilities. *Meteor. Monogr.*, **57**, 9.1–9.15.

Mishchenko, M. I., 2000: Calculation of the amplitude matrix for a nonspherical particle in a fixed orientation. *Appl. Opt.*, **39**, 1026–1031.

Morrison, H. C., M. R. Kumjian, C. P. Martinkus, O. P. Prat, and M. van Lier-Walqui, 2018: A generalized *n*-moment normalization method for deriving raindrop size distribution scaling relationships. *J. Appl. Meteor. Climatol.*, **conditionally accepted**.

Petäjä, T., and Coauthors, 2016: BAECC: A field campaign to elucidate the impact of biogenic aerosols on clouds and climate. *Bull. Amer. Meteor. Soc.*, **97**, 1909–1928.

Pfeifer, M., G. C. Craig, M. Hagen, and C. Keil, 2008: A polarimetric radar forward operator for model evaluation. *J. Appl. Meteor. Climatol.*, **47**, 3202–3220.

Prat, O. P., and A. P. Barros, 2007: Exploring the use of a column model for the characterization of microphysical processes in warm rain: Results from a homogeneous rainshaft model. *Adv. Geosci.*, **10**, 145–152.

Prat, O. P., and A. P. Barros, 2009: Exploring the transient behavior of $Z-R$ relationships: Implications for radar rainfall estimation. *J. Appl. Meteor. Climatol.*, **48**, 2127–2143.

Prat, O. P., A. P. Barros, and F. Y. Testik, 2012: On the influence of raindrop collision outcomes on equilibrium drop size distributions. *J. Atmos. Sci.*, **69**, 1534–1546.

Prat, O. P., A. P. Barros, and C. R. Williams, 2008: An inter comparison of model simulations and VPR estimates of the vertical structure of warm stratiform rain during TWP-ICE. *J. Appl. Meteor. Climatol.*, **47**, 2797–2815.

Pruppacher, H. R., and R. L. Pitter, 1971: A semi-empirical determination of the shape of cloud and rain drops. *J. Atmos. Sci.*, **28**, 86–94.

Putnam, B. J., M. Xue, Y. Jung, N. Snook, and G. Zhang, 2014: The analysis and prediction of microphysical states and polarimetric radar variables in a mesoscale convective system using double-moment microphysics, multinetwork radar data, and the ensemble Kalman filter. *Mon. Wea. Rev.*, **142**, 141–162.

Putnam, B. J., M. Xue, Y. Jung, G. Zhang, and F. Kong, 2017: Simulation of polarimetric radar variables from 2013 CAPS Spring Experiment storm-scale ensemble forecasts and evaluation of microphysics schemes. *Mon. Wea. Rev.*, **145**, 49–73.

Ryzhkov, A. V., M. R. Kumjian, S. M. Ganson, and A. P. Khain, 2013a: Polarimetric radar characteristics of melting hail. Part I: Theoretical simulations using spectral microphysical modeling. *J. Appl. Meteor. Climatol.*, **52**, 2849–2870.

Ryzhkov, A. V., M. R. Kumjian, S. M. Ganson, and P. Zhang, 2013b: Polarimetric radar characteristics of melting hail. Part II: Practical implications. *J. Appl. Meteor. Climatol.*, **52**, 2871–2886.

Ryzhkov, A. V., M. Pinsky, A. Pokrovsky, and A. P. Khain, 2011: Polarimetric radar observation operator for a cloud model with spectral microphysics. *J. Appl. Meteor. Climatol.*, **50**, 873–894.

Sachidananda, M., and D. Zrnić, 1986: Differential propagation phase shift and rainfall rate estimation. *RS*, **21**, 235–247.

Schenkman, A. D., M. Xue, A. Shapiro, K. Brewster, and J. Gao, 2011: The analysis and prediction of the 8-9 May 2007 Oklahoma tornadic mesoscale convective system by assimilating WSR-88D and CASA radar data using 3DVAR. *Mon. Wea. Rev.*, **139**, 224–246.

Schrom, R. S., and M. R. Kumjian, 2018: Bulk-density representations of branched planar ice crystals" Errors in the polarimetric radar variables. *J. Appl. Meteor. Climatol.*, **57**, 333–346.

Sinclair, V. A., D. Moisseev, and A. von Lerber, 2016: How dual-polarization radar observations can be used to verify model representation of secondary ice. *J. Geophys. Res.*, **121**, 10 954–10 970.

Sisterson, D. L., R. A. Peppler, T. S. Cress, P. J. Lamb, and D. D. Turner, 2016: The ARM Southern Great Plains (SGP) Site. *Meteor. Monogr.*, **57**, 6.1–6.14.

Sulia, K. J., and M. R. Kumjian, 2017a: Simulated polarimetric fields of ice vapor growth using the adaptive habit model. Part I: Large-eddy simulations. *Mon. Wea. Rev.*, **145**, 2281–2302.

Sulia, K. J., and M. R. Kumjian, 2017b: Simulated polarimetric fields of ice vapor growth using the adaptive habit model. Part II: A case study from the FROST experiment. *Mon. Wea. Rev.*, **145**, 2303++2323.

Szyrmer, W., S. Laroche, and I. Zawadzki, 2005: A microphysical bulk formulation based on scaling normalization of the particle size distribution. Part I: Description. *J. Atmos. Sci.*, **62**, 4206–4221.

Testud, J., S. Oury, R. A. Black, P. Amayenc, and X. Dou, 2001: The concept of "normalized" distribution to describe raindrop spectra: A tool for cloud physics and cloud remote sensing. *J. Appl. Meteor.*, **40**, 1118–1140.

Thurai, M., V. N. Bringi, M. Szakáll, S. K. Mitra, K. V. Beard, and S. Borrmann, 2009: Drop shapes and axis ratio distributions: comparison between 2D video disdrometer and wind-tunnel measurements. *J. Atmos. Oceanic Technol.*, **26**, 1427–1432.

Thurai, M., G. J. Huang, V. N. Bringi, W. L. Randeu, and M. Schönhuber, 2007: Drop shapes, model comparisons, and calculations of polarimetric radar parameters in rain. *J. Atmos. Oceanic Technol.*, **24**, 1019–1032.

Tokay, A., A. Kruger, and W. F. Krajewski, 2001: Comparison of drop size distribution measurements by impact and optical disdrometers. *J. Appl. Meteor.*, **40**, 2083–2097.

Tong, M., and M. Xue, 2005: Ensemble Kalman filter assimilation of Doppler radar data with a compressible nonhydrostatic model: OSS Experiments. *Mon. Wea. Rev.*, **133**, 1789–1807.

Willis, P. T., 1984: Functional fits to some observed dropsize distributions and parameterization of rain. *J. Atmos. Sci.*, **41**, 1648–1661.

Xie, X., R. Evaristo, S. Trömel, P. Saavedra, C. Simmer, and A. Ryzhkov, 2016: Radar observation of evaporation and implications for quantitative precipitation and cooling rate estimation. *J. Atmos. Oceanic Technol.*, **33**, 1779–1792.

Yoneyama, K., C. Zhang, and C. N. Long, 2013: Tracking pulses of the Madden-Julian Oscillation. *Bull. Amer. Meteor. Soc.*, **94**, 1871–1891.

LIST OF FIGURES

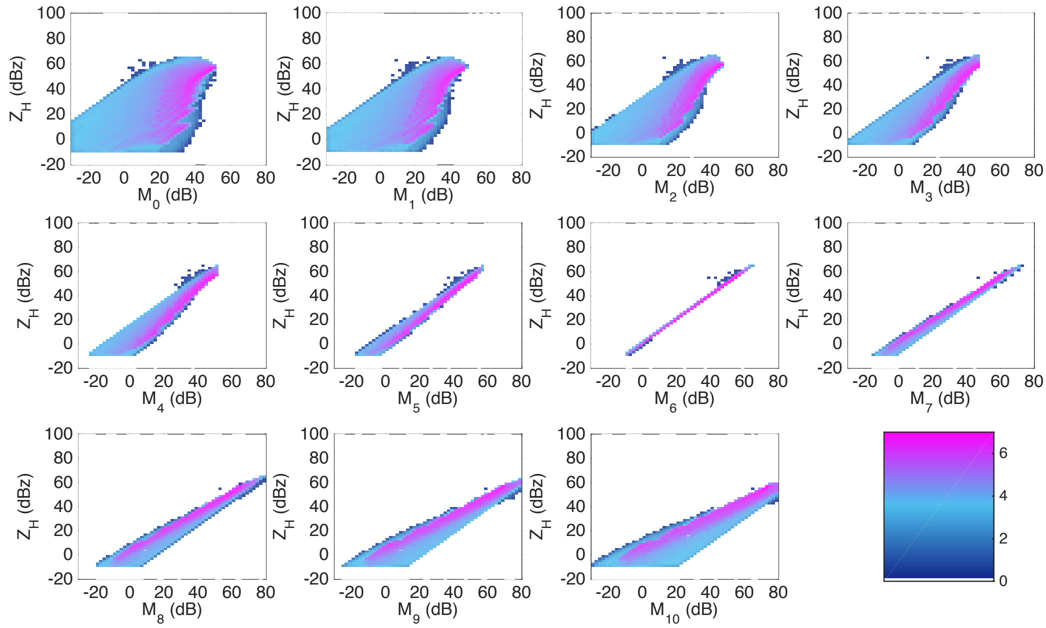

FIG. 1. Joint histograms of moments M_k and Z_H, for k from 0 to 10 inclusive, all in dB. Color shading indicates the base-10 logarithm of count, according to scale.

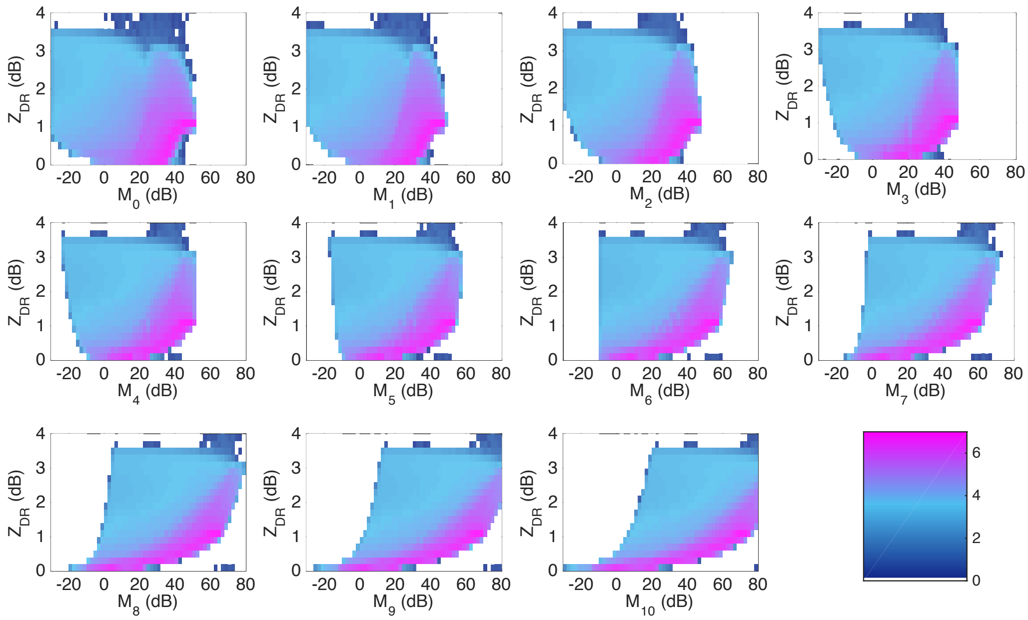

681 FIG. 2. Joint histograms of moments M_k and Z_{DR}, for k from 0 to 10 inclusive, all in dB. Color shading
682 indicates the base-10 logarithm of count, according to scale.

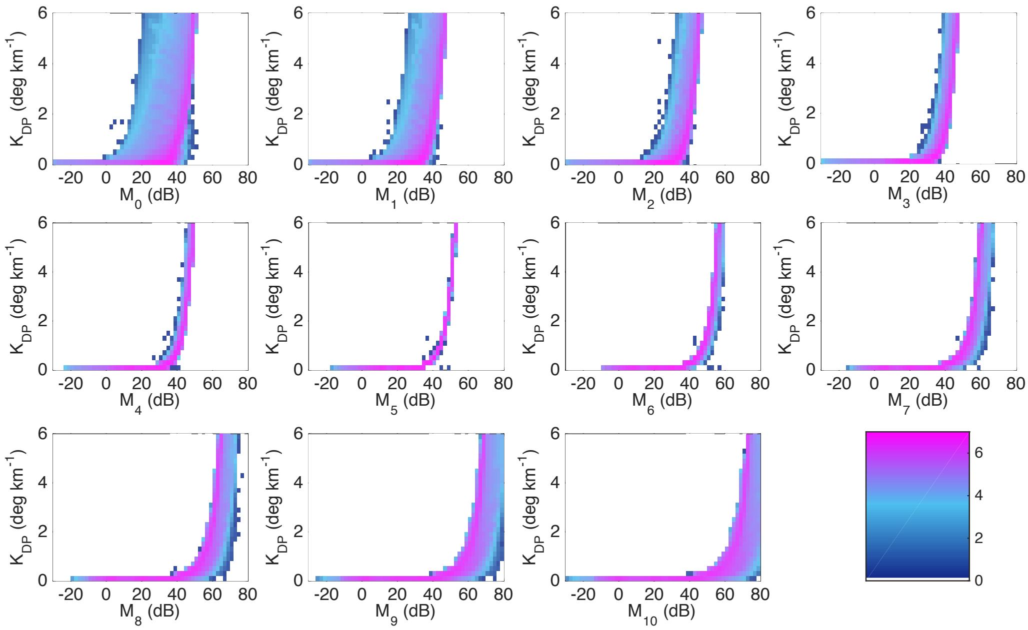

683 FIG. 3. Joint histograms of moments M_k and $K_{\rm DP}$, for k from 0 to 10, inclusive, in dB and deg km^{-1},
684 respectively. Color shading indicates the base-10 logarithm of count, according to scale.

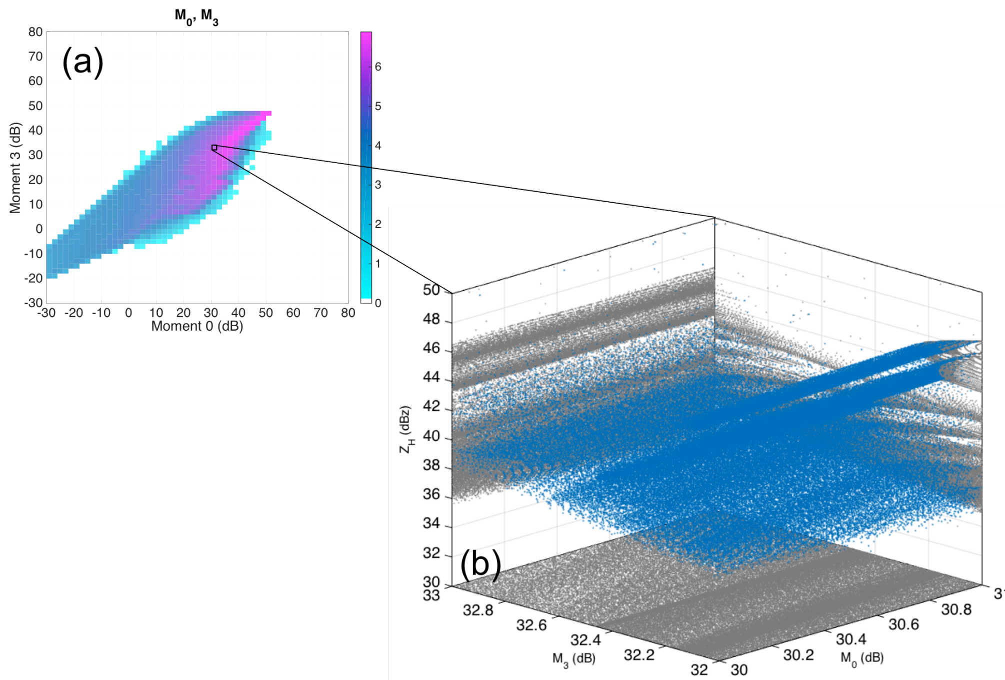

FIG. 4. Joint distribution of M_0 and M_3 (both in dB) for the entire DSD dataset, shading indicating occurrence in logarithmic scale. An arbitrary bin is selected (black square). Outset: All Z_H values within the selected M_0-M_3 bin are shown in three dimensions (blue markers) along with their two-dimensional projections (gray markers on lateral walls of outset).

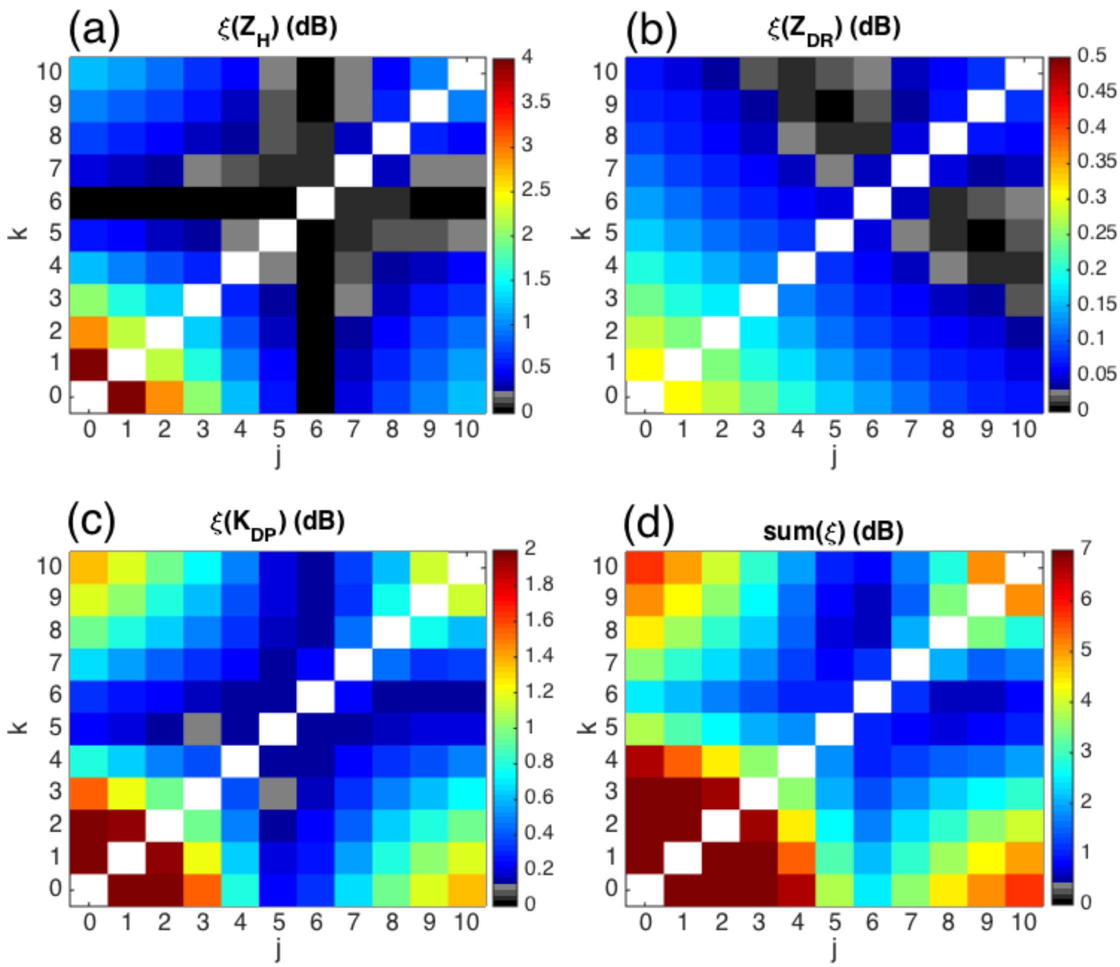

FIG. 5. (a) $\xi(Z_H)$ (dB), (b) $\xi(Z_{\mathrm{DR}})$ (dB), (c) $\xi(K_{\mathrm{DP}})$ (dB), and (d) sum of ξ (dB) for the subsampled dataset as a function of moment orders j and k. Larger values indicate more variability for that moment combination. White values indicate no values. Note that these matrices are symmetric.

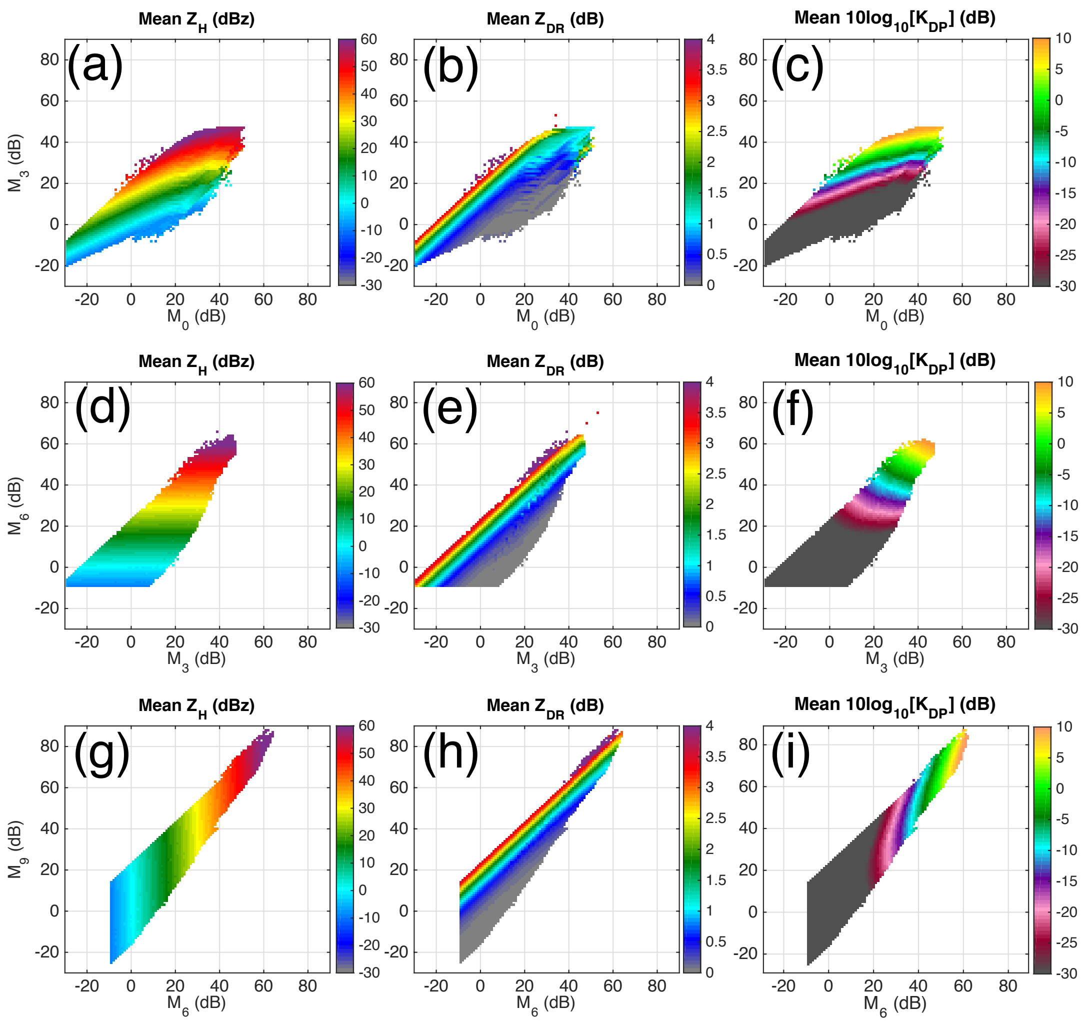

FIG. 6. Graphical representation of different two-moment forward operators. Top row (a-c) is the M_0, M_3 forward operator, middle row (d-f) is M_3, M_6, and bottom row (g-i) is M_6, M_9. Left column is Z_H, middle column is Z_{DR}, right column is K_{DP}.

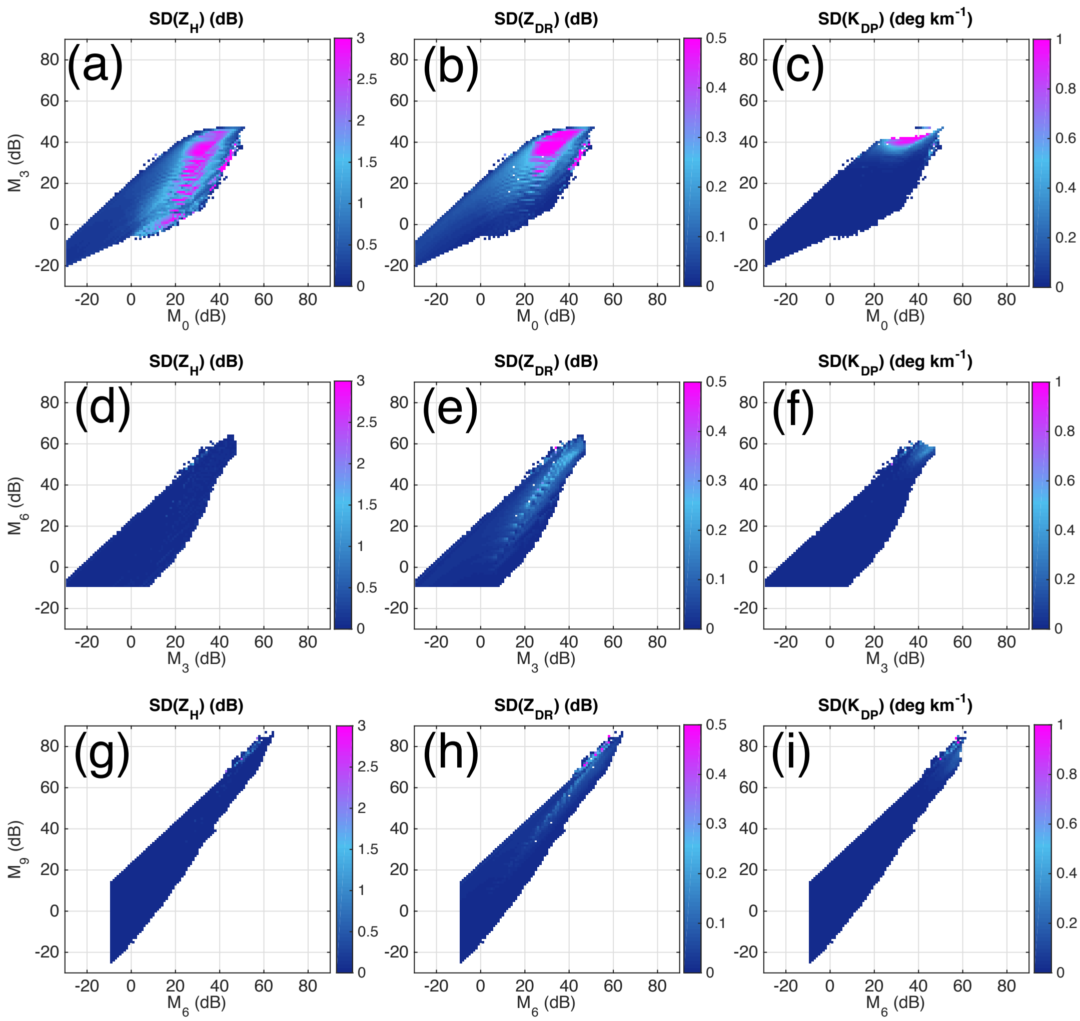

695 FIG. 7. As in Fig. 6, but here the standard deviation of the distribution of radar variable values within each
696 pixel is shown.

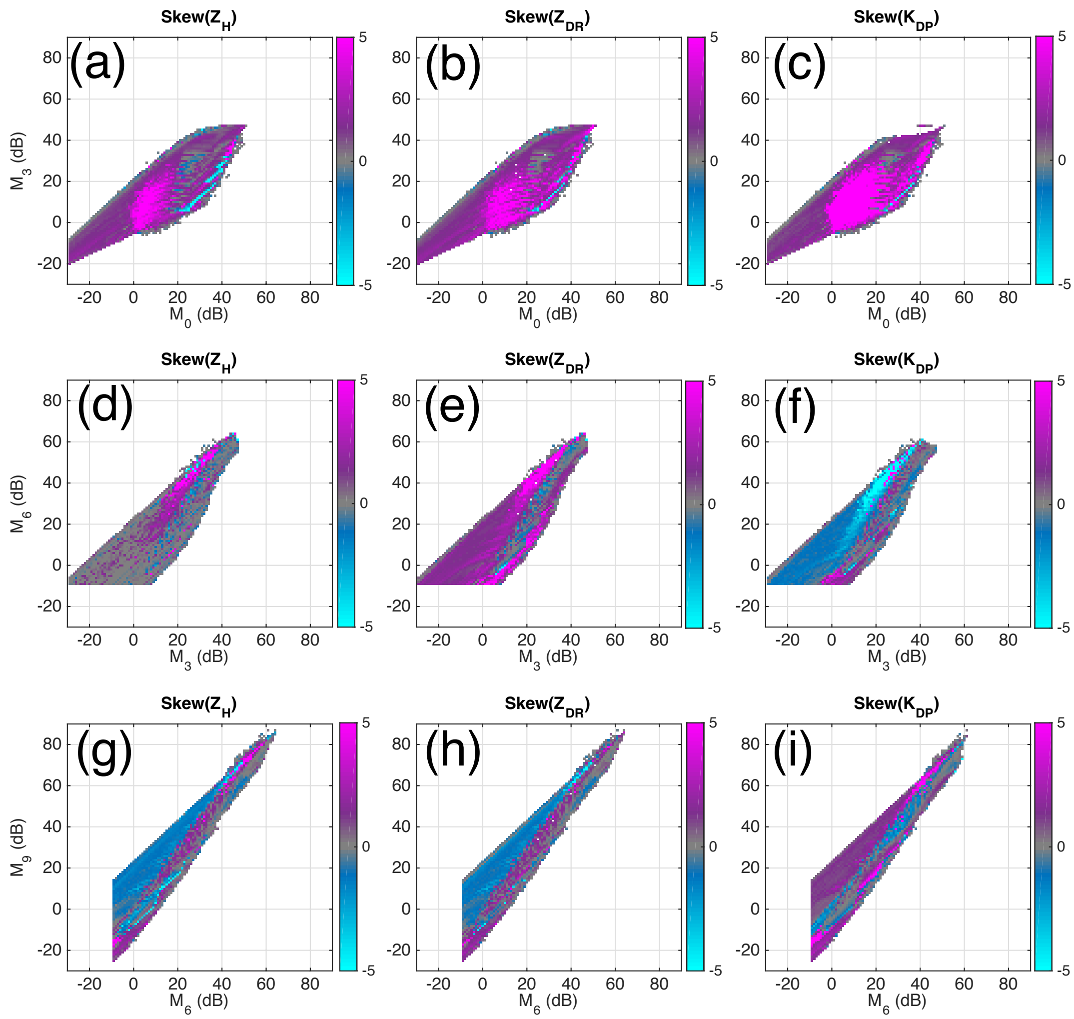

FIG. 8. As in Fig. 7, but here the skewness of the distribution of radar variable values within each pixel is shown.

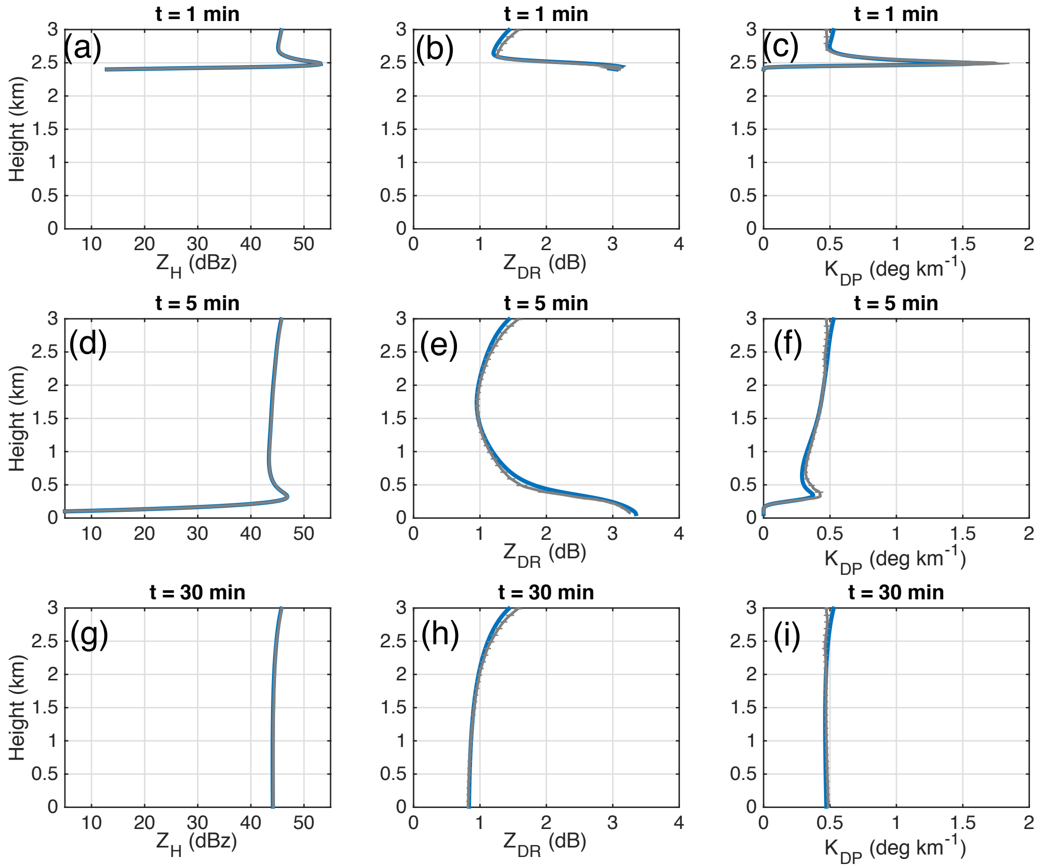

FIG. 9. Example output of forward operator compared to "truth" from bin model (blue).M_6-M_9 forward operator shown (gray), with error bars indicating ± 1 standard deviation. The model is initialized with a gamma DSD aloft with 36.7 mm hr^{-1} rainfall rate, with rows corresponding to output times 1, 5, and 30 minutes.

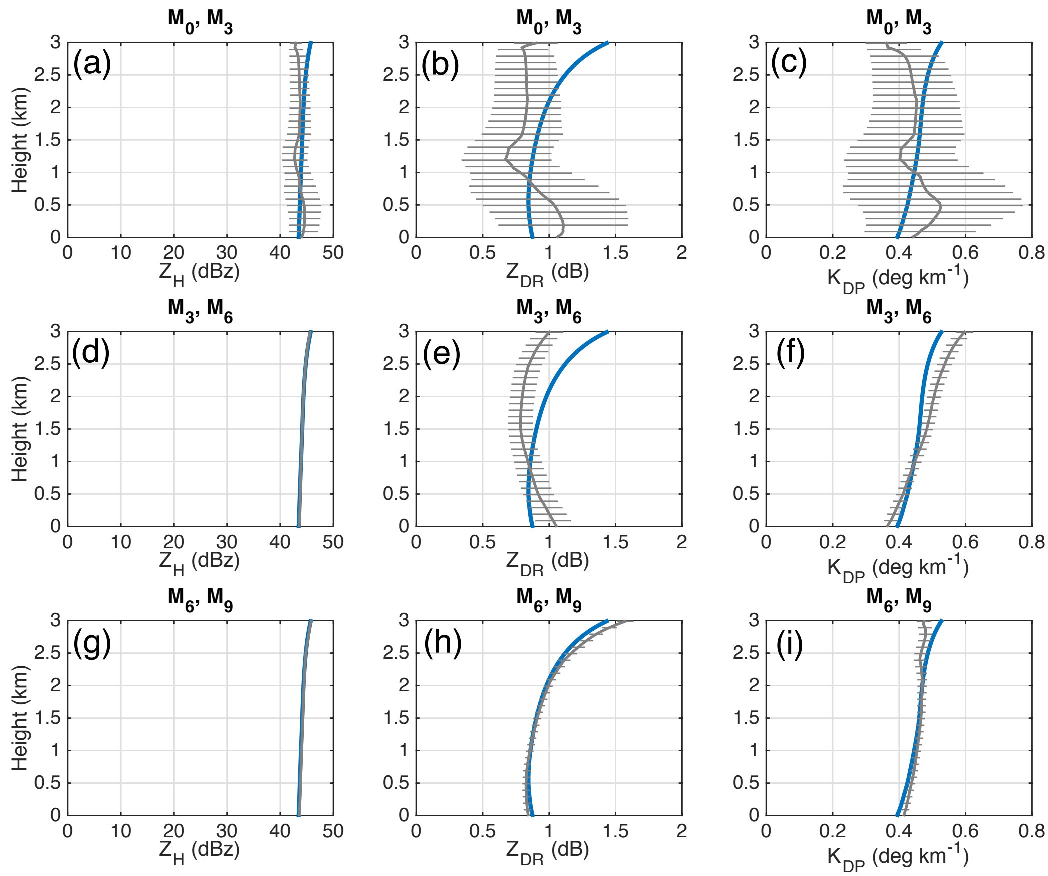

FIG. 10. Comparison of different versions of two-moment forward operators for the simulation shown in Fig. 9, but for an output time 10 minutes. Each row now corresponds to different operator: M_0-M_3, M_3-M_6, and M_6-M_9. columns are Z_H, Z_{DR}, and K_{DP}.

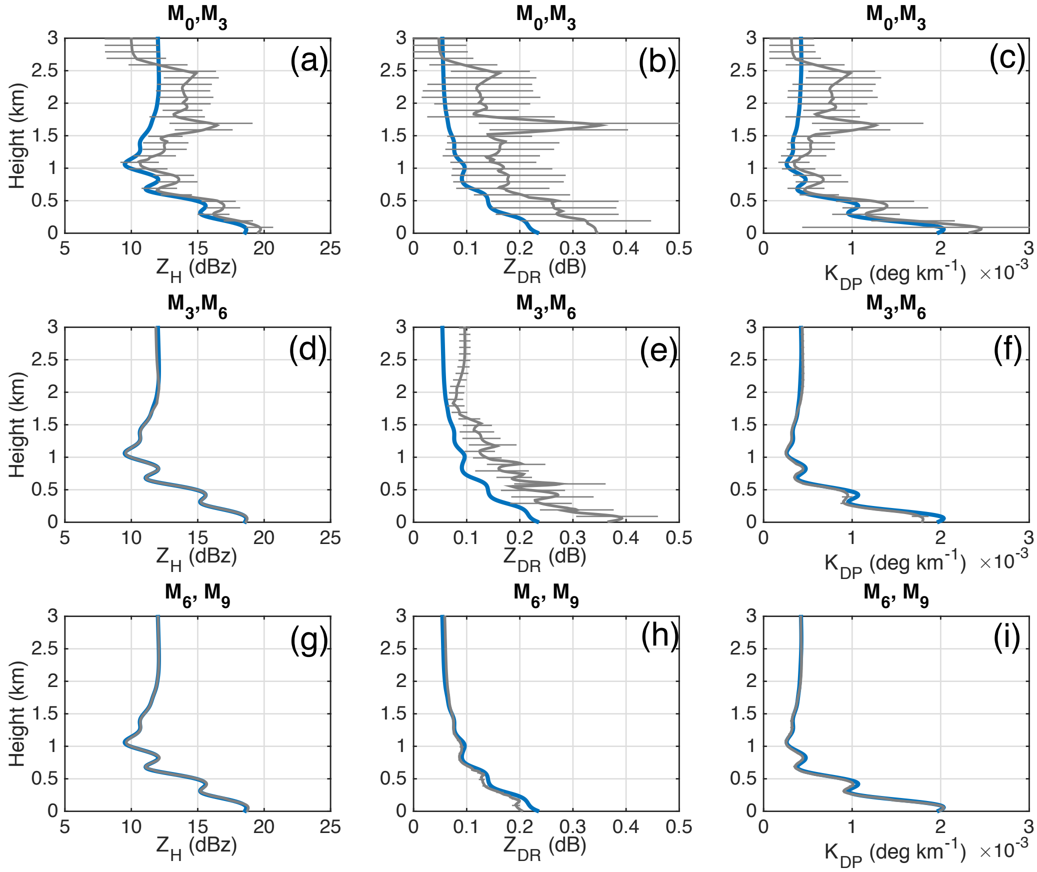

FIG. 11. As in Fig. 10, but for a simulation initialized with a gamma DSD with rainfall rate of 0.3 mm hr^{-1}. Each row now corresponds to a different operator: M_0-M_3, M_3-M_6, and M_6-M_9. columns are Z_H, $Z_{\rm DR}$, and $K_{\rm DP}$.